Tribology and Materials
Vol. 3, No. 1, 2024, pp. 1-14

ISSN 2812-9717
https://doi.org/10.46793/tribomat.2024.003

Study of the wear process in an experimental simulation of a fuselage/runway rubbing contact

Tovignon DEVO [1,2,3,*], Arnaud BEAURAIN [2,4], Eric DELETOMBE [1,2], Yannick DESPLANQUES [2,3,4]

[1] ONERA – The French Aerospace Lab, Lille, France
[2] UMR 9013, CNRS, Lille, France
[3] Centrale Lille, Lille, France
[4] University of Lille, Lille, France
*Corresponding author: williamdevo@yahoo.fr

Keywords
emergency landings
high-energy friction
pad-on-disc
wear
third body
multi-scale

History
Received: 30-09-2023
Revised: 25-12-2023
Accepted: 27-12-2023

Abstract

In this work, the authors tackle the problem of laboratory simulation of frictional contact in wheels-up emergency landing conditions. To design a novel tribometer simulating the contact between an aircraft structure and a runway, one must carry two complementary main tasks: the understanding of the underlying physical mechanisms and the scaling up of the in-lab results to the scale of interest. The authors propose to progress on the first task by conducting exploratory work using existing resources. Their contribution consists of a multi-scale methodology to reconstruct the wear process in a tribological system within wheels-up emergency landing conditions. This could provide guidance for safer aircraft and runway design. The study falls within the framework of three-body tribology. The proposed multi-scale characterisation methodology is made up of four steps. After describing the whole tribological system, its mechanical response is measured and analysed. This measurement is complemented by surface observations and physicochemical analyses. Finally, all the measurements and observations are discussed to come across a phenomenological wear scenario that revealed friction and wear as system responses with the key role of the third body.

1. Introduction

Over the past ten years, the Bureau of Aircraft Accidents Archives has recorded in Europe more than fifty accidents without fatalities. In these emergency situations, the European Union Aviation Safety Agency (EASA) recommends to land with "the wheels retracted (where applicable)" [1]. The aircraft thus approaches the runway, lands and then slides onto the runway when its horizontal deceleration is predominant. This study focuses on this sliding phase (herein referred to as a wheels-up emergency landing), from a tribological point of view. The parts of aircraft structure most exposed to runway friction are the fuselage and engine nacelles, never too far from fuel zones.

This work is licensed under a Creative Commons Attribution-NonCommercial 4.0 International (CC BY-NC 4.0) license

The available documents [2,3] report on the risks due to wear and heating phenomena affecting the aircraft and exposing fuel tanks to puncture, with a fire risk that can endanger the passenger's safety. To continue improving aeronautical safety, it is thus vital to carry out a tribological study to identify and understand the underlying physics beneath those phenomena. This is actually part of a larger study the objective of which is the understanding and characterisation of the thermomechanical behaviour of aircraft's structure during wheels-up emergency landings or crash situations [4].

This research is not simple, partly because full-scale experiments are not possible at this stage of the study. Neither analytical nor numerical solutions are available to assess the tribological performances of an aircraft while sliding on a runway. Experimental laboratory simulations are explored in this study. The problem (Fig. 1) remains

a complex matter, especially as no academic background studies currently exist.

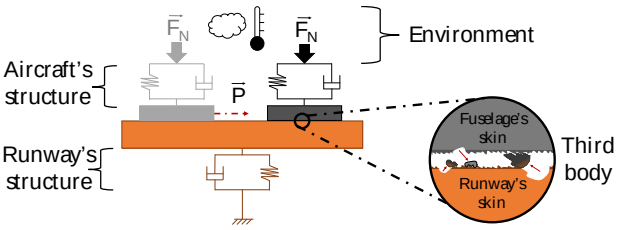

Figure 1. Schematic of a tribological system involved in a wheels-up emergency landing; adapted from Devo [5], licensed under Etalab Open License 2.0

The work presented in this paper aims to provide a phenomenological understanding of the wear process to guide the construction of a lab-scale tribometer capable of simulating emergency situations. The choices of the framework and means of the study were made based on the literature.

The study of a wear process may ideally fall within the framework of three-body tribology and follow the third-body approach [6,7]. The material definition of the third body leads to the notion of contact debris. The contact scenario according to Godet is specified in [8]. First, it is a matter of particles pull-out (third body formation mechanisms). These particles are then trapped in the contact and form beds between the two rubbing materials. A steady state may then be established, consisting of the detachment and removal of these particles. This vision was enriched by Yves Berthier with the description of the third body's kinetics in the contact process zone (different material flow in a tribological circuit) [9]. The wear process thus depends on the tribological circuit which depends on the third body [10] but also on the rubbing parts [11]. The influence of the mechanical [12] and physicochemical environment [13] on the tribological circuit must also be taken into account.

The study framework being defined, the in-lab characterisation of any wear process must then be conducted on a tribometer. Based on past accidents, the ranges of interest defined in [4] for apparent contact pressure, sliding speed and duration are respectively 0.5 – 5 MPa, 10 – 70 m/s and 5 – 50 s. As no device is yet dedicated to the study, the authors' strategy was to use a device "that closely simulates a tribosystem of interest" as recommended in the ASTM G115 standard [14].

2. Materials and methods

Among the numerous existing devices dedicated to friction study [15-26], the pad-on-rotating disc tribometer available at the LaMcube Lab [27] was chosen. Despite the rotating movement of the disc, it seemed to be a good compromise with respect to the orders of magnitude of speed and apparent pressure. At a later stage, the wear process is generally identified from an interpretation of macroscopic mechanical measurements of a normal load and a friction force [28]. Moreover, the physicochemical wear mechanisms driving the friction occur at lower scales and are related to the nature of the material pairs, the sliding speed and the applied load [11].

In brief, in this paper, based on the literature review, the authors propose to study and characterise the wear process in a tribological system based on a pad-on-rotating disc tribological experiment, within wheels-up emergency landing conditions of load and speed. The novelty lies in the nature of the studied materials and the conditions of high speed and load. The tribological system studied in this paper is made up of a first body (pad), a counter-body (disc), the mechanical and physicochemical environment (structural factors of stiffness, surfaces, geometry, etc.), the mechanical actions (sliding speed, load, etc.), the characteristics of the ambient environment (temperature, humidity) and a third body (the set of interfacial elements generated during the contact).

2.1 Description of the rubbing parts

The pad is made from a runway material (concrete) and the disc is from an aircraft structure material (2024-T3 aluminium). The 2xxx series of aluminium alloys are widely used in the aerospace industry for their mechanical properties. The 2024-T3 is one of the most common alloys used in fuselage structures.

The pad used in this experiment is made by water jet cutting a civil engineering concrete block obtained from the ONERA in Lille. It was 11 ± 1 mm thick. One of its flat surfaces was glued to a stiff steel support which was then fixed to the part of the tribometer dedicated to the load application. The surface parallel to the previous one was set to be put in contact with the disc during the test. It was milled by hand to reduce its roughness and to slope the apparent contact surface by approximately 3°. This was done to facilitate a flat adjustment of the pad and disc surfaces. The apparent contact area is approximately 10 cm^2 (internal and external radii of 92 and 108 mm, respectively and an angle of 39°).

As the initial chemical composition of the pad was not known, various chemical measurements (EDX and XRD) were carried out to reveal its composition [5]. The pad is essentially made of calcium (Ca) and silicon (Si). XRD measurements revealed calcium carbonate ($CaCO_3$) and quartz (SiO_2) as the main chemical species present in the pad. Aragonite ($CaCO_3$ with traces of Sr, Pb and Zn) and iron oxide (Fe_2O_3) are also present in smaller quantities.

The disc used is obtained by a water jet cutting of a raw plate. Its total thickness was 3.6 ± 0.1 mm. The plate from which the disc was cut off was made up of a 2024-T3 aluminium alloy core, each side being coated with a thin layer of pure aluminium. This 130 ± 10 µm thick coating (Fig. 2) generally serves to protect the core of the material from corrosion. The core is a structural hardening alloy with an ISO AlCu4Mg1 chemical composition and the indication T3 refers to a thermal tempering heat treatment.

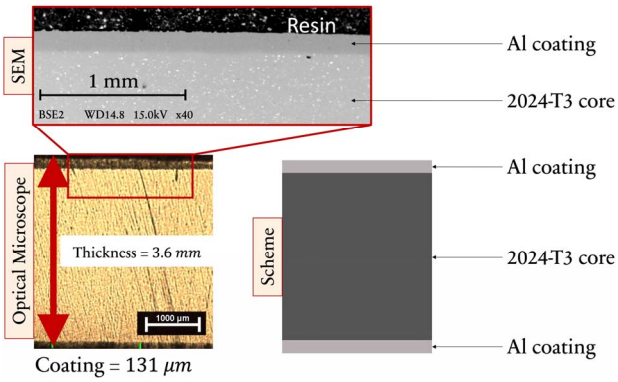

Figure 2. Partial observation of a cross-section of the disc, using an optical microscope (OM) and scanning electron microscope (SEM); adapted from Devo [5], licensed under Etalab Open License 2.0

2.2 Description of the tribometer

The used tribometer is shown in Figures 3 and 4. It consists of two parts dedicated to the rotation of the disc and the application of the load by the pad. The spindle rotates the disc by means of an electric motor. A flywheel is installed at the exit of the motor to study transient speed regimes, and in this research, the spindle was driven at constant speed.

The load cell allows the application of a normal load by the pad on the disc. It consists of an actuator composed of a slider guided by two elastic arms; the whole assembly forms a deformable parallelogram. What is more, a loading spring whose compression is controlled by a linear actuator allows the load application to the mobile plate. A 3D piezoelectric force sensor is mounted on the plate and then the pad and its support are mounted on it (measurements are thus only taken close to the contact; nevertheless, the fluctuations measured are representative of the vibrations of the whole pad and its support). The piezoelectric force sensor is protected by a cooling circuit just in case the pad heats up, during the test.

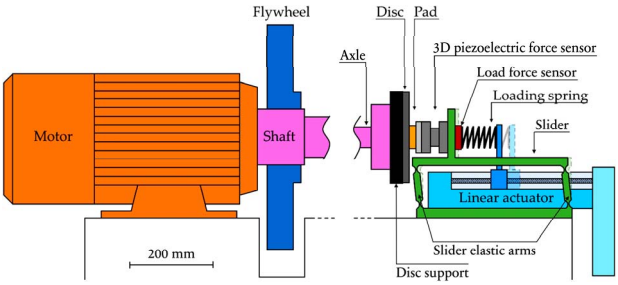

Figure 3. Schematic of the LaMcube's pad-on-rotating disc tribometer; adapted from Davin et al. [29], licensed under CC BY 4.0

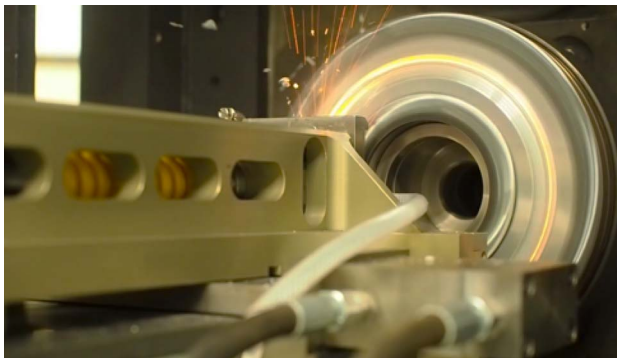

Figure 4. LaMcube's pad-on-rotating disc tribometer during a test; reprinted from Devo [5], licensed under Etalab Open License 2.0

The load force sensor allows the control of the normal load through the measurement of the load applied by the loading spring, while the piezoelectric force sensor, mounted close to the contact, provides the normal, tangential and radial contact forces. Also, the load provided by the spring allows the bending of the spring's arms. This bending force is therefore dependent on the position of the plate to make the pad/disc contact. The force available for loading the contact is therefore the result of the force supplied by the spring and the force required to move the plate.

The disc is mounted on two circular supports, on its outer and inner perimeters. The pad is in contact with the disc along an intermediate radius of the disc between these supports. Thus, the normal load induces a bending deformation of the disc. The disc is fixed to its support by 12 screws, 6

on the outer perimeter and 6 on the inner perimeter (Fig. 5). The bending stiffness of the disc assembly thus varies circumferentially, with the disc almost clamped at the fixings, and in simple supports between the fixings.

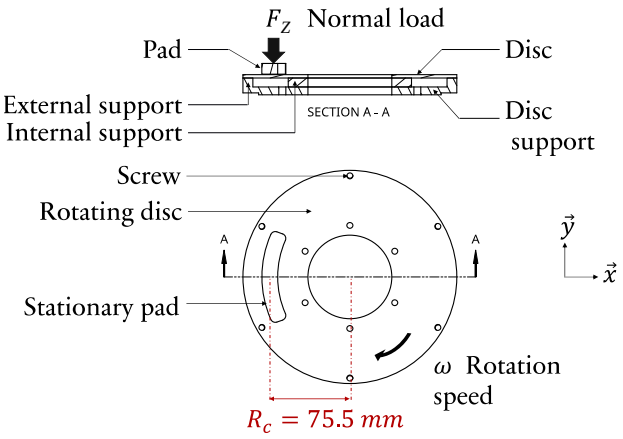

Figure 5. Outline schematic of a pad-on-rotating disc tribological test; adapted from Devo [5], licensed under Etalab Open License 2.0

The pad is positioned so that its centre is at a distance of R_c = 75.5 mm from the centre of the disc (Fig. 5). As the pad and the disc do not have the same curvature, the rubbed surface is wider than the pad. The median cross-section of the pad is positioned equidistant between the disc's supports, whereas due to the curvature of the pad, the cross-section at its end is shifted towards the external support of the disc.

2.3 Test parameters

During the test, the motor is power-driven with a constant rotation speed ω set value equal to 1990 rpm (which gives the tangential speed of approximately 16 m/s). After each revolution, the speed of the flywheel is measured and a compensating motor torque is used to adjust the power with respect to the set value. The spring is controlled in displacement to reach, in this case, a constant load F_Z set value of 900 N during 20 s. The values of the test parameters are depicted in Figure 6.

The evolution of the disc's rotation speed signal (Fig. 6) reveals three main phases between the beginning and the end of the contact. There is a run-in phase (contact establishment) in which the speed decreases for about 1.4 s, a speed accommodation phase in which the speed increases to its nominal set value for about 4.6 s and a phase in which the speed set value is reached (the speed is thus constant for about 13.8 s).

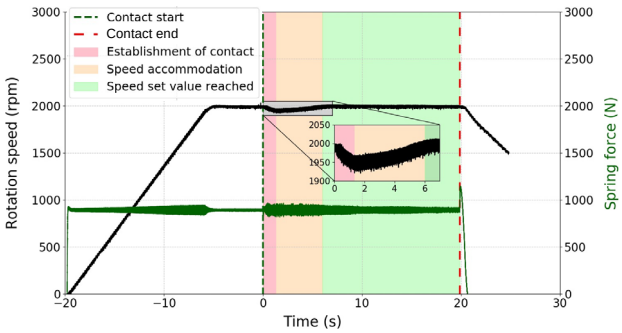

Figure 6. Time evolution of the disc's rotation speed and spring force signals during the test; adapted from Devo [5], licensed under Etalab Open License 2.0

The spring is preloaded to the nominal set value of force before the first contact ($t \approx 0$ s). The pad surface is placed at 0.2 to 0.3 mm from the disc surface. By bending the elastic arms (Fig. 3), the pad is brought into contact with the disc. After the contact starts, the spring force value slightly fluctuates around the nominal set value.

3. Results

3.1 Mechanical response of the system

The available 3D piezoelectric sensor allows the acquisition of normal, radial and tangential forces with a frequency of 100 kHz. Only the normal and tangential force responses will be considered here. The evolution of the tangential force (representative of the friction force) is presented in Figure 7. It thus depicts the friction force as a function of time, number of revolutions and angular position. Negative values are taken on, which can be explained by the dynamic contribution of the pad and its support (the real force at the contact is the difference between the measured force and the dynamic resultant induced by the tangential acceleration of the pad/support assembly).

Figure 7 highlights the effect of the angular variation in the stiffness of the disc. Although it decreases, the friction force is high by the stiffest sections of the disc. The normal force evolves in the same way.

The angular position is represented by the number of measuring points per revolution. As the speed varies during the first 6 s, the number of values acquired is not constant from one revolution to another. This variation is characterised by a frequency shift (Fig. 8). The post-processing of the force signals is deepened by exploiting its temporal but also frequency evolution during the contact.

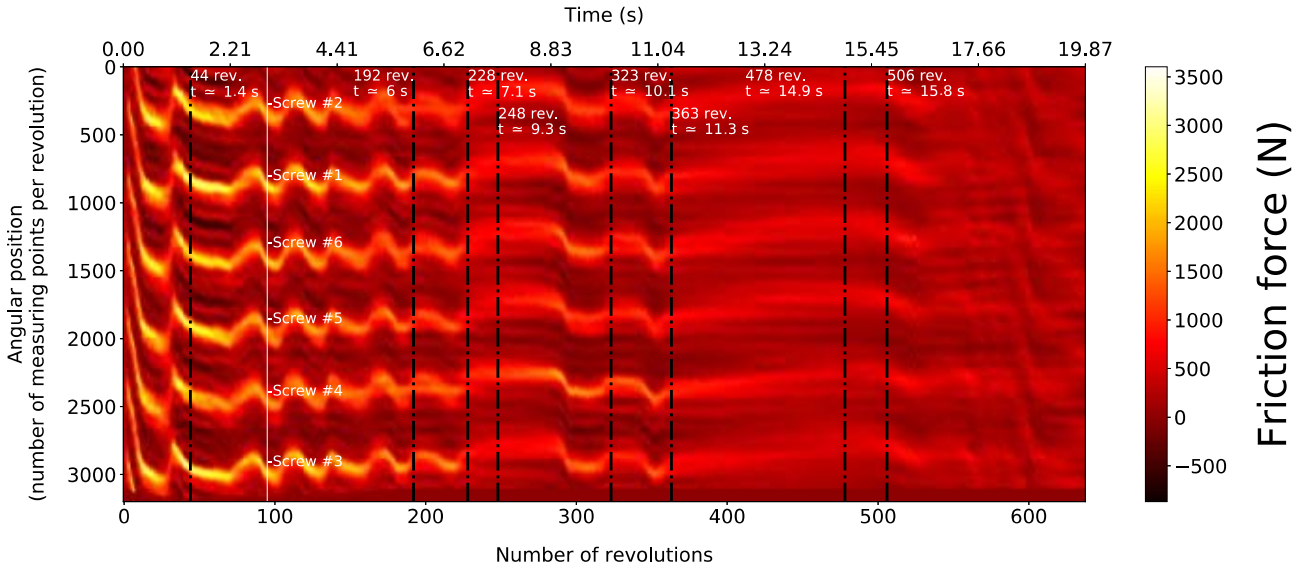

Figure 7. Evolution of the friction (tangential) force signal during the test, as a function of time, revolution and angular position of the disc; adapted from Devo [5], licensed under Etalab Open License 2.0

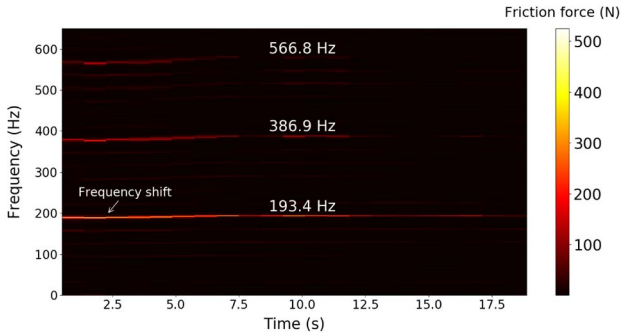

Figure 8. Time/frequency diagram of the friction (tangential) force signal during the test; adapted from Devo [5], licensed under Etalab Open License 2.0

Modal analysis of the idle tribometer revealed that the first vibration mode of the tribometer occurs around a frequency of 1 kHz which is very high compared to the 32 Hz disc rotating frequency (f_{rot}), so it is not ludicrous to assume the tribometer is sufficiently rigid not to disrupt the test.

The time/frequency diagrams of the normal and friction forces signals are very similar spectra (Fig. 8). The frequency analysis of the friction force reveals three energetic frequencies. The most energetic one is 193.4 Hz corresponding to the 6th harmonic of the mean rotating frequency f_{rot}. This $6 \times f_{rot}$ frequency is characteristic of the bolted mounting of the disc (i.e. 6 tribological events of stiffness variation occur during one disc revolution).

The two other energetic frequencies correspond to the 12th and 18th harmonics of f_{rot} (386.9 and 566.8 Hz). The tribological events associated with these frequencies are not identified. However, these two frequencies can be considered as the 2nd and 3rd harmonics of the first energetic frequency ($6 \times f_{rot}$).

The frequency analysis of the mechanical response in force highlights the preponderance of the angular variation of the disc's bending stiffness; thus, illustrating the importance of taking structural factors into account in the description and characterisation of the tribosystem. Figure 9 depicts the evolution of the normal and friction forces signals after having isolated the contributions of the three frequencies mentioned previously (contribution of stiffness).

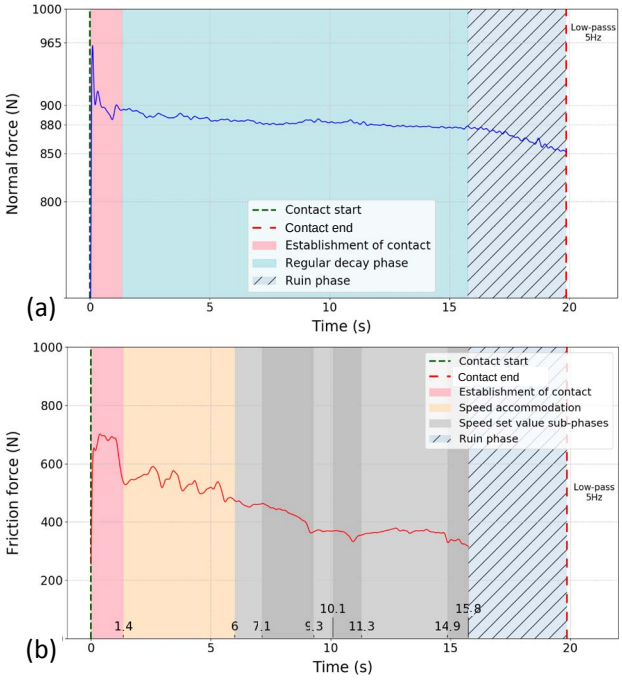

Figure 9. Time evolution of the: (a) normal force and (b) friction force; adapted from Devo [5], licensed under Etalab Open License 2.0

The normal force evolves in time with respect to three phases (Fig. 9a). In the first phase of contact establishment, the normal force has a maximum at 965 N at $t \approx 0.3$ s and then decreases uncontrollably until 900 N at $t \approx 0.9$ s.

The second phase lasts until $t \approx 15.8$ s, where the normal force decreases in a regular way until 880 N. This 20 N decrease in the normal force available to the contact corresponds to the increase in the force provided by the spring for the translation of the plate and is necessary to maintain the contact.

It should be remembered that the test is carried out with a constant spring force and that part of this force is required to bend the elastic arms guiding the plate to make contact. The stiffness of this bond being 0.3 N/µm, approximately 67 µm must be covered to maintain contact during this phase of the test. This stroke can be explained by the accommodation of the rubbing parts or the increase in the bending of the disc. Indeed, the increase in the temperature of the disc during the test leads to a decrease in the stiffness of the aluminium alloy and therefore in the bending stiffness of the disc.

The third phase corresponds to the decrease of the contact, where the normal force decreases until the end of the contact. The uncontrollable wear of the pad (observed post-mortem) is undoubtedly responsible for this brutal decrease in normal force. This breakage of the pad marks the end of the test; it was chosen not to consider the experimental data beyond $t \approx 15.8$ s in the analysis of this test.

The time evolution of the friction force is analysed (Fig. 9b) with respect to multiple phases. In the contact establishment phase, the friction force rises to 700 N and then oscillates between this value and 680 N before dropping to 530 N at $t \approx 1.4$ s. This is the beginning of the speed accommodation phase in which five cycles of increase/decrease of the tangential force follow each other to reach a value of 460 N at $t \approx 6$ s. In the third phase (set of grey sub-phases) where the speed is fairly steady, the friction force progressively decreases to 315 N. Levels are observed from around 6 to 7 s, then from around 9 to 11 s and finally from around 11 to 15 s.

The frequency analysis was also performed for the spindle torque signal [5]. As the force signals are sufficient to illustrate the method presented in this paper, the complementary analysis of the torque signal is not exploited.

3.2 Multiscale analysis of the parts wear

The infrared (IR) camera used is a FLIR SC7000 Series (SC7600-7650) with a 25 mm lens and a maximum resolution of 640 × 512 pixels. It allowed the observation of the rubbed surface of the disc during the test, with a frequency of 2 images per revolution (only one half of the disc is presented in Figure 10). At this stage, it is important to note that the infrared radiation of an object depends on the temperature and the emissivity of its surface. Thus, an infrared image contains 2 pieces of information that are sometimes difficult to separate, as for rubbed surfaces, wherein the temperature and the emissivity vary simultaneously.

It is nevertheless possible to qualitatively interpret the temporal evolution of IR images in terms of thermal localisation, as a local rise in temperature is revealed by a diffuse image, with the spread of the heat produced by friction; whereas a variation of the IR image without diffusion is representative of a local variation of the emissivity of the surface, which can make it possible to identify the recycled flow third body captured by the disc for example.

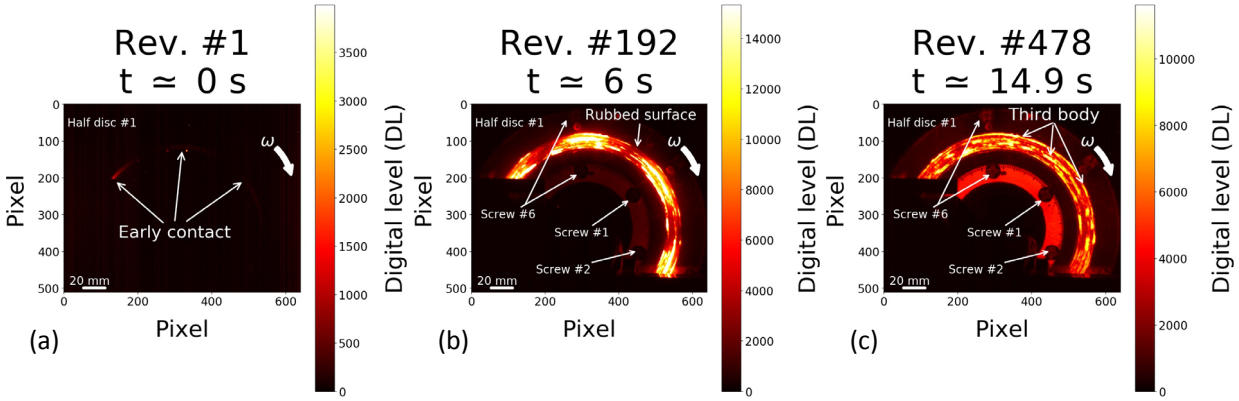

Figure 10. Infrared images of the 1st half of the disc (screws #1, #2 and #6) within different disc revolutions: (a) 1st revolution, $t \approx 0$ s, (b) 192nd revolution, $t \approx 6$ s and (c) 478th revolution, $t \approx 14.9$ s; adapted from Devo [5], licensed under Etalab Open License 2.0

The location of the contact during the first 6 seconds was thus identified. At $t \approx 0$ s, the first areas of contact are established in the areas of highest stiffness by the fixing screws (Fig. 10a) and the friction was more intense there. The disc's rubbed surface extends throughout the test but energy dissipation by friction remains more intense by the fixings (Fig. 10b at $t \approx 6$ s).

Two key information can be deduced from the IR exploitation: the history of the location of the energy dissipation (radial and circumferential) and the history of the development of the third body. The observation of the rubbed surface in the IR also highlights the high local contrast of the IR image (Fig. 10c at $t \approx 14.9$ s) which is characteristic of an emissivity contrast of the surface. As shown below, this contrast is induced by the development of a solid third body on the disc (and the pad) which is partly recycled by the disc after each revolution.

The worn surfaces of the rubbing parts (disc and pad) were observed post-mortem for further understanding. As a result of the end of the contact, the third body is spread out between the disc and the pad (source, internal and recycled third body's material flows included). The third body produced by the contact (and not ejected into the wear flow) is also observed and analysed post-mortem. To these ends, macro photographs of the worn disc and pad surfaces were taken for morphological surface analysis (Fig. 11).

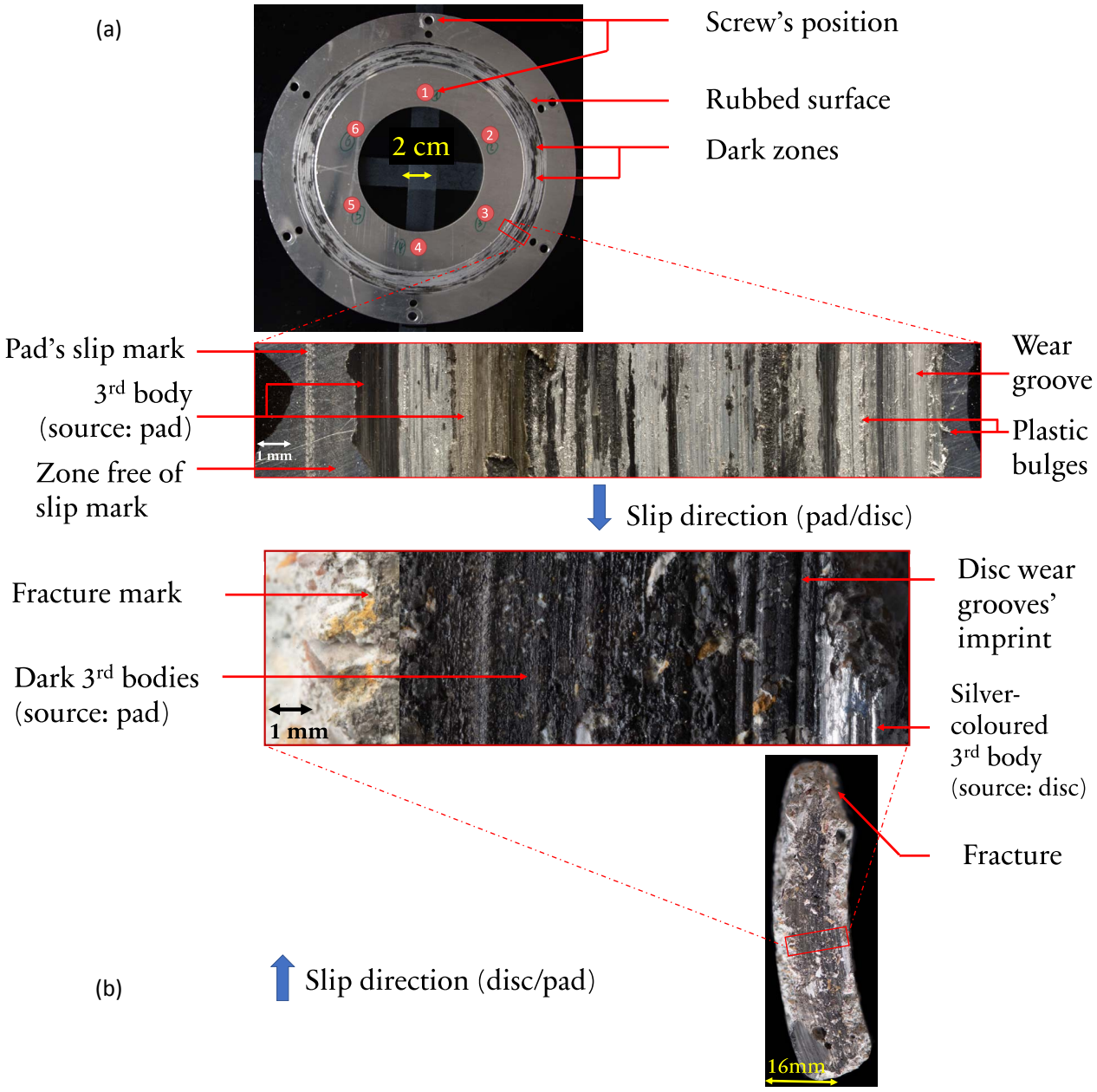

Figure 11. Reconstruction of the rubbed surfaces of the: (a) disc and (b) pad; adapted from Devo [5], licensed under Etalab Open License 2.0

The degradation of the pad is macroscopically observable post-mortem (Fig. 11b). The fracture marks, which are free of slip marks and the observed third body are clues to associate the pad's ruin with the last moments of the test. The surface of the pad left with wear marks is covered by a layer of dark third bodies (generated from the pad) also observed on the surface of the disc. A silver-coloured third body (generated from the disc) is also observed. The slipping tracks left by the disc are oriented in the direction of sliding.

Figure 11a shows that the disc's rubbed surface is worn heterogeneously, radially but also circumferentially, which is consistent with the contact locations observed with the IR camera. The observation of the track is detailed in an area of the disc fixing, as this region is representative of all the wear mechanisms that have been observed.

This observation shows that the surface is heterogeneously covered with third bodies and that contact is not established over the entire width of the track. The slip mark left by the pad on the outer perimeter of the disc (Fig. 11a) and the surface still free of slip marks confirm this last point. Plastic deformations (displaced material) and wear grooves reveal local abrasive wear of the disc surface. These wear grooves have left their opposite imprint on the pad, due to the surfaces adjustment. The third body observed on the surface of the disc nevertheless differs visually from those observed on the pad (grey, beige and dark, as in Figure 11a).

The morphological analysis of the surface of the disc is deepened observing a cross-section chosen to be transverse to the sliding surface to reveal the diversity of the wear mechanisms. SEM observation in backscattered electrons (BSE) mode (Fig. 12a), reveals the initial protective Al coating and the depth of the mechanisms. The abrasion of the surface has locally generated wear grooves deep down to the 2024 substrate. The plastic deformation of the Al coating also generates bulges. The result is protuberances whose height exceeds the thickness of the Al coating, and which are locally covered by a third body of several tens of µm. It is relevant to note that their morphology reveals a ductile fracture in the material but also that they are free of any trace of slip. Thus, after its formation, the displaced material did not directly contribute to the adjustment of the contact.

The detailed observation (Figs. 12b, 12c and 12d) reveals that the third body is made of layers, the lower ones being powdery while the upper layers are compact and have been part of the slip surface.

Physicochemical analysis is a means of determining the origin of the solid third body. Post-mortem EDX measurements on the pad's surface revealed the preponderance of calcium (Ca), silicon (Si) and aluminium (Al) in its chemical composition. EDX measurements were also carried out on the surface and a cross-section of the disc [5]. As with the pad, they revealed the preponderance of Ca, Si and Al chemical elements. The cross-sectional measurement allowed the isolation of the third body from the disc and to see that it is essentially made of Ca and Si. This is in line with the hypothesis that the solid third body is mainly produced by the pad.

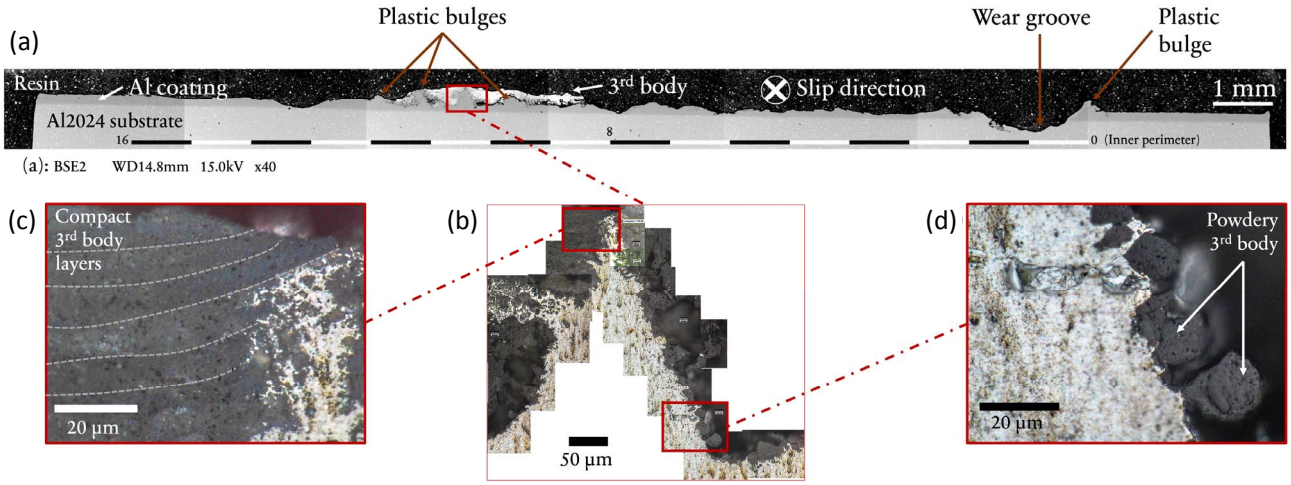

Figure 12. Microscopic observations: (a) observation of a cross-section of the disc in a transverse direction of the slip (SEM composite image), (b) observation of a plastic bulge (OM composite image) and (c) and (d) details of the third body in the vicinity of a plastic bulge (OM composite image); adapted from Devo [5], licensed under Etalab Open License 2.0

To verify this hypothesis, micro-XRD measurements were carried out in [5] to identify chemical compounds. It turns out that the solid third body is essentially made of calcium carbonate ($CaCO_3$), quartz (SiO_2), larnite (Ca_2SiO_4), gehlenite ($Ca_2Al(AlSiO_7)$) and hatrutite ($Ca_2(SiO_4)O$). These compounds are derived from the former chemical composition of the concrete pad.

4. Discussions

The solid debris that came out of contact are essentially chip-like debris from the aluminium disc and broken pieces of the concrete pad that were recovered post-mortem with clips or by hand. The recovered debris were then weighed: the chip-like debris have a mass of 0.111 ± 0.001 g and the concrete pieces had a mass of 2.226 ± 0.001 g. The total mass of debris recovered post-mortem is thus 2.337 ± 0.002 g.

The disc's initial mass was 299.2 ± 0.001 g and as it weighs 311.85 ± 0.001 g at the end of the test, the disc has thus gained 12.65 ± 0.002 g. The post-mortem rubbed surface of the disc is covered by dark zones that are in fact solid third bodies. Assuming that the mass gain of the disc is due to the presence of various solid bodies, one understands that the mass of the chip-like debris cannot simply be considered as the mass lost by the disc. That is to say, the establishment of the mass balance (as a characteristic of wear) of the aluminium disc is not straightforward. The disc's wear is not synonymous with its loss of mass, the mass being the result of a balance between the material lost and gained by the disc. The study and analysis of the solid third body thus become essential to establish a reasonable wear process scenario.

4.1 Reconstitution of the wear process and third bodies formation

A phenomenological wear scenario is proposed to describe the wear process and the formation history of the studied solid third body. The results showed that the pad and the disc produce the third bodies and thus feed together the source flow of material in the tribological circuit. Analysis of the debris ejected from the contact showed that the chip-like debris produced by the abrasion of the disc contribute significantly to the wear flow (a wear flow corresponding to the material amount which once and for all leaves the contact). In addition, analysis of the IR images indicated that the chip-like debris ejection is mainly active at the beginning of the test, during the contact establishment phase. The abrasive wear has left a rubbed track on the disc thus marked by grooves and bulges, while debris (Al, AlCu4Mg1) adhere locally to the surface of the pad and thus contributes to the internal material flow of the third body. Moreover, the pad produced a dark powdery third body which largely covers its surface. This third body also covers heterogeneously the disc's surface while being locally compacted under the action of contact. This third body had thus contributed significantly to the internal flow.

Table 1, which overviews the chemical compounds present in the tribological system, shows that the third body is made up of chemical elements coming from the disc and pad materials, as well as new elements coming from the friction between these two materials.

Table 1. Chemical compounds present in the tribosystem

Tribosystem element	Disc	Pad	Third body
Chemical compounds	Al, AlCu4Mg1	$CaCO_3$, SiO_2, Fe_2O_3	$CaCO_3$, SiO_2, Ca_2SiO_3, Ca_2SiO_4, $Ca_3(SiO_4)O$, Ca_3SiO_5, $Ca_2Al(AlSiO_7)$, Al, AlCu4Mg1

The thickness variation of the disc mainly affected the aluminium coating, reaching locally the AlCu4Mg1 substrate. Considering the height of the grooves, the thickness of the whole disc has gained locally by the top of the displaced material up to 240 µm and lost up to 130 µm in the valleys (Fig. 13).

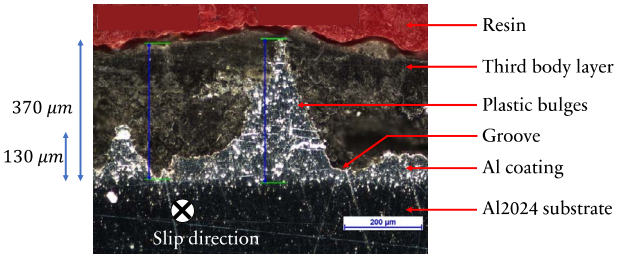

Figure 13. OM observation of a third body covering a bulge (the disc's cross-section being transverse to the direction of sliding); adapted from Devo [5], licensed under Etalab Open License 2.0

The powdery third body is trapped in the valleys in the vicinity of the displaced material. Its flow into the contact, driven by the rotation of the disc, led to a segregation of the third body

particles, the coarsest (up to 15 µm in diameter, Fig. 12d) being sustained in-depth in the valleys while the finest particles accumulate on the surface (where the slip is accommodated) constituting compact layers under the pressure of the contact (sedimentation, Fig. 12c).

The history of the third body's formation (at meso- and microscopic scales) is essential for understanding these processes and the tribological behaviour of the system. For example, the thickness of the third body can reach several hundred µm, which is much greater than the thicknesses generally observed (3 µm in [19], 10 µm in [13], for example). The third body shown in Figure 13 covers a 370 µm high bulge which was produced by the plastic flow of the aluminium coating of an initial thickness of 130 µm. It is noted that this bulge sustained its initial morphology of a ductile fracture during the slip. Thus, it has not undergone any compressing, whereas the surrounding third body has been compacted by the contact action.

Thus, the third body superseded the first and counter-body to adjust the load bearing capacity of the contact. Hence, it had been subjected to very high mechanical and thermal stresses, and when the temperature rose in the contact, thermochemical reactions might have occurred and could explain the appearance of new chemical compounds in the constitution of the third body. Shearing could also explain that appearance, but this has not been investigated in this paper.

For example, larnite (Ca_2SiO_4) appears at temperatures between 600 and 800 °C [30] and pressures between 9 and 13 GPa [31]. An extensive search for larnite would allow the definition of thermal mapping by micro-XRD. Based on the larnite's thermodynamic characteristics, Figure 14 (right) depicts the larnite detection areas on the rubbed surface, i.e. areas where the maximum temperature reached was at least 600 °C. A correlation can thus be made between the physicochemical measurements and temperature.

This is consistent with the assumption of the load bearing capacity of the third body, which thus reduces the direct contact between the disc and the pad in the areas of larnite presence. The establishment of the third body consequently protects the disc by reducing abrasive wear. This protective role of the third body thus limits the wear of aluminium and therefore its loss of thickness. The generated solid third body constantly interacts with the first body, counter-body and the environment of the tribological system.

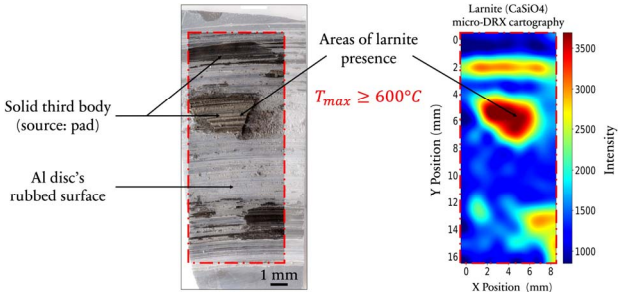

Figure 14. Partial observation of the disc's rubbed surface in photograph (left) and in post-mortem cartography of micro-XRD measurement spectra (right); adapted from Devo [5], licensed under Etalab Open License 2.0

4.2 Reconstitution of the multiscale phenomenological contact scenario

The development of the identified protective third body partially reduced the structure's initial bearing capacity. The rest of the tribosystem adjusts itself to it. As this load-carrier third body has been dispersed over the disc's surface, it is relevant to associate it with an evolution of the contact location during sliding.

An effective friction radius is thus defined by the ratio of the torque and the friction force. This novel indicator monitors the evolution of the location of the friction during the test. Figure 15 depicts this effective radius; the inner and outer perimeters of the rubbed track are indicated to appreciate its evolution in contact.

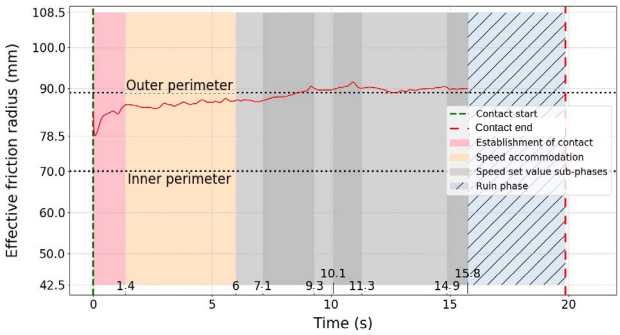

Figure 15. Evolution of the effective contact radius, from an energy dissipation point of view, with respect to the rubbed track; adapted from Devo [5], licensed under Etalab Open License 2.0

The effective radius oscillated significantly in the uncontrollable phase of contact establishment. From the phase of speed accommodation, it increased quite regularly to establish itself by the outer perimeter during the rest of the test. The evolution of the effective radius thus expresses a

radial migration of the energy dissipation towards the outside of the track. Correlations can be established between its evolution and the appearance of the rubbed track.

In the cross-section in Figure 12a, the presence of abrasion grooves across the entire width of the track is associated with the uncontrollable phase of the first moments of contact. In fact, the oscillation of the effective friction radius, the high friction (Fig. 9b) and the ejection of chip-like debris correspond to the formation of these grooves by abrasive wear. The development of the dark third body is associated with the migration of the effective friction radius towards the outside of the track. The abrasion grooves on the inner track are relieved of the third body, while the third body covers the grooves on the outer track. The migration of the contact went with a significant decrease in friction force (Fig. 9b) which can be associated with the development of a bearing capacity by the third body and stabilisation of friction corresponding to the stabilisation of the effective radius on the outer perimeter.

The contact scenario evolves throughout the test. To reconstruct a tribological scenario, all elements of the system must be considered. A phenomenological contact scenario is thus proposed from the measurements/observations in the tribosystem.

The polar diagrams in Figure 16 depict the friction force measured at a specific time as a function of the angular position of the pad on the disc. The chronological reading direction of a revolution is counterclockwise, with the angular origin of a diagram corresponding to the first instant of contact. The three diagrams presented are representative of friction evolution in the phases of contact establishment (Fig. 16a), speed accommodation (Fig. 16b) and when the speed set value is reached (Fig. 16c).

Each diagram shows 6 friction force lobes associated with the pad passing by the disc-fixing screws. The mounting of the disc was deliberately flexible so that structural stiffness effects could be considered in the experiment. The inner and outer circumferential supports allowed radial bending of the disc (between the supports), the bending stiffness of the assembly being greater in the vicinity of the 6 pairs of disc-fixing screws. Also, the arc covered by the pad is 39°, i.e. it can be inscribed entirely between 2 consecutive clamping planes of the disc.

Thus, the 6-lobe diagrams can be interpreted by the passage of the pad, the circumferential variation of stiffness inducing a circumferential variation of the deflection of the disc, which thus leads to an undulatory deformation of the track in the slip direction, from the point of view of the pad.

A lobe can thus be broken down into 3 phases: a sudden increase in the friction force corresponds to a bow effect, when the pad's contact entrance climbs a peak of the undulation; an intermediate phase when the middle part of the pad crosses a peak of the undulation, the decreasing friction force (disappearance of the bow effect) fluctuates differently from one lobe to another and from one turn to another; then a rapid decrease in the friction force as the pad's contact exit descends into a valley of the undulation. The turning points between each lobe correspond to the transition of the pad from one peak to the next one.

These diagrams are consistent with the 6-lobe polar diagrams of the normal force (Fig. 17), the normal force being maximum when the pad is in line with the disc clamping planes, minimum between 2 clamping planes. The fluctuation of the normal force puts the fluctuation of the friction force into perspective.

These results (discussed further in [5]) illustrate the importance of considering the structure in the adjustment of a sliding contact, with regard to friction, wear and the tribological circuit. Indeed, the passage of the pad in the valleys corresponds to instants of low normal load, thus possible contact openings (circumferential) from the entrance to the exit of the pad, a favourable factor to the circulation of the third body (internal and recycled flows).

The lobe evolution varies from one phase of the test to the other. In the contact establishment phase (Fig. 16a) at the very beginning of the contact, the variable intensity of the friction lobes of a revolution is explained by the initial differences in the relative position and orientation of the 2 surfaces (pad and disc), varying and exacerbating the bow effect from one lobe to the other. It should be noted that this bow effect favours wear by abrasion and is consistent with the high friction force during this initial phase of the test.

In the speed accommodation phase (Fig. 16b) the friction lobes become uniform over one revolution, which can be explained by an adaptation of the rubbed track, on the one hand by abrasive wear and on the other hand by the plastic deformation of the disc which limits the amplitude of its undulatory deformation. This accommodation

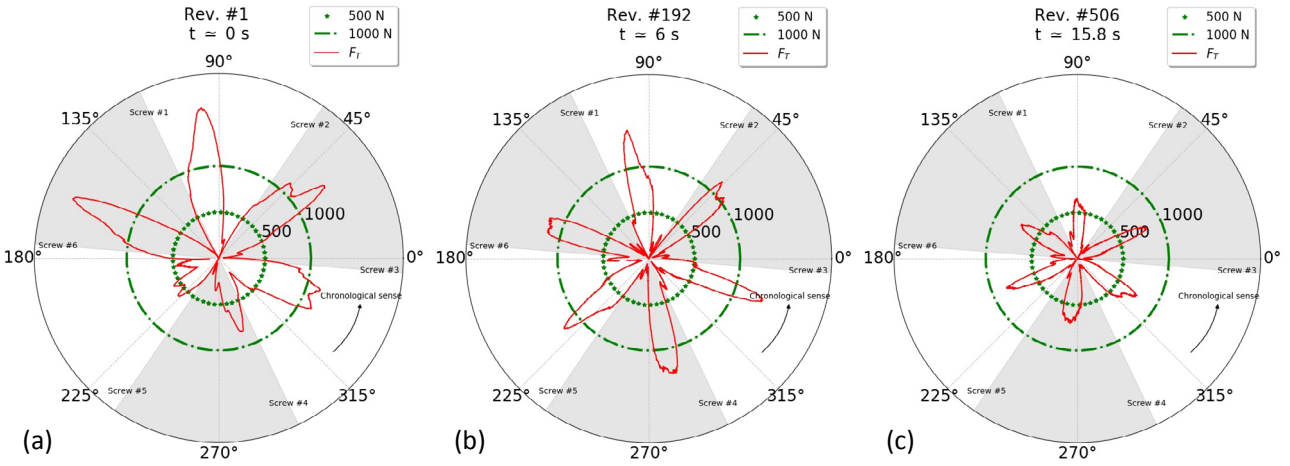

Figure 16. Angular evolution of the raw measured tangential force signal during different revolutions of the disc (green circles represent iso-value curves at 500 and 1000 N): (a) 1st revolution, $t \approx 0$ s, (b) 192nd revolution, $t \approx 6$ s and (c) 506th revolution, $t \approx 15.8$ s; adapted from Devo [5], licensed under Etalab Open License 2.0

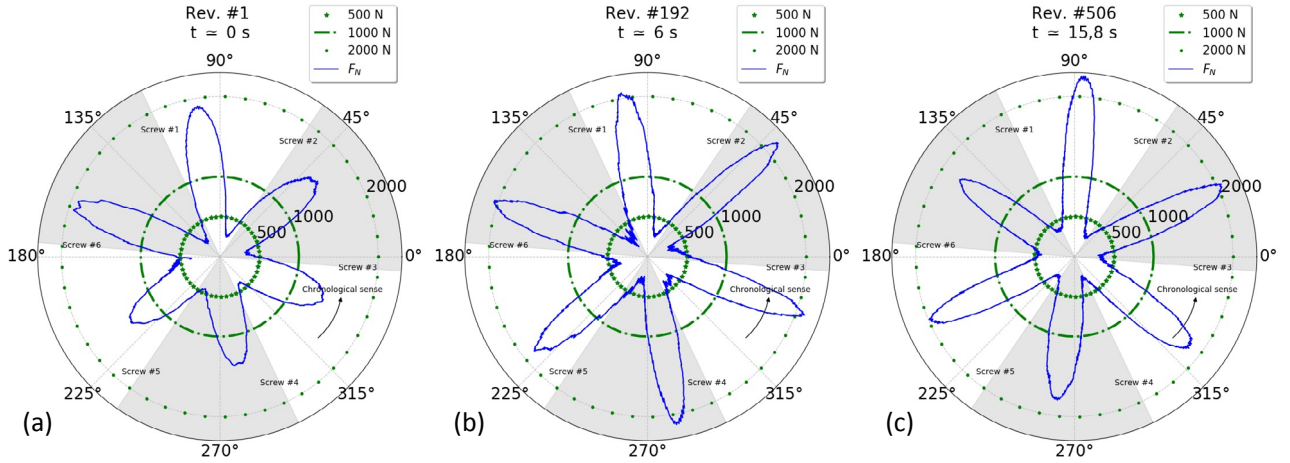

Figure 17. Angular evolution of the raw measured normal force signal during different revolutions of the disc (green circles represent iso-value curves at 500, 1000 and 2000 N): (a) 1st revolution, $t \approx 0$ s, (b) 192nd revolution, $t \approx 6$ s and (c) 506th revolution, $t \approx 15.8$ s; adapted from Devo [5], licensed under Etalab Open License 2.0

also explains the gradual decrease in the intensity of the lobes, with the decrease in abrasive wear in favour of the establishment of sliding on the third body which develops in the contact. The oscillations in the tangential force observed in Figure 9 correspond to the alternation between the development of the third body in the contact (decrease in friction force) and the formation of abrasion grooves (growth in friction force).

In the speed set value phase (Figure 16c) the amount of third body present in the contact has reached a sufficient value to ensure the essential bearing capacity and slip. The decrease in frictional force in this phase (Fig. 9b) is consistent with the decrease in lobe intensity.

5. Conclusions

In this first exploratory work of its kind, an existing pad-on-rotating disc tribometer was employed to simulate a frictional contact within conditions close to a wheels-up emergency landing. The key findings are as follows:

- The third body, by its nature and dimensions, protects the disc structure. It partly bears the load and limits the diffusion of frictional heat towards the disc. Such a mechanism could therefore limit the thickness loss and heating of an airframe around fuel tanks during a wheels-up emergency landing.
- The strong influence of the structure (bolted mounting) on the tribological response was highlighted. The angular evolution of the friction (which is more intense in the vicinity of the fixings) confirmed that the structural aspects are of first order in the tribological process.
- The proposed framework and methodology allow the multiscale and multiphysics

characterisation of the wear process in a pad-on-rotating disc tribological system. It consists of a reconstruction of a contact scenario based on a macroscopic analysis complemented by surface observations and physicochemical measurements.

These findings are very promising and need to be enriched with further learning from a more advanced tribometer. It would allow the study of more tribological scenarios, highlighting various wear processes. The relative heat dissipation in the pad and disc could also be thoroughly investigated.

Acknowledgements

The present research work has been supported by the PHYSAFE project financed by the DGAC and ELSAT2020 project co-financed by the European Union with the European Regional Development Fund, the French State and the Hauts de France Region Council. The authors gratefully acknowledge the support of these institutions.

The authors are also very grateful to D. Joly (ONERA) for his help in studying the structural factors of the system and to Pr. P. Roussel and al. for the XRD and micro-XRD measurements at the Univ. Lille, CNRS, LaMcube Lab, UMR 8181 – UCCS – Unité de Catalyse et Chimie du Solide, F-59652 Villeneuve d'Ascq.

References

[1] CS-25 Amendment 23, Certification Specifications and Acceptable Means of Compliance for Large Aeroplanes, European Aviation Safety Agency, 2019.

[2] Investigation Report BFU 15-1354-AX, Bundesstelle für Flugunfalluntersuchung, Braunschweig, 2015.

[3] Final Report, Accident No 1400/11, Aircraft B-767-300ER, SP-LPC, State Commission on Aircraft Accidents Investigation, Warsaw, 2011.

[4] E. Deletombe, J. Berthe, G. Portemont, T. Fourest, F. Coussa, D. Joly, T. Devo, M. Ragonet, A. Peignon, Study and Characterization of the Dynamic Response of Material for the Improvement of Crash Behavior of Aircraft Structures, ONERA, Lille, 2020.

[5] T.W.G. Devo, Étude et caractérisation de l'usure et l'échauffement des matériaux structuraux aéronautiques en cas d'atterrissage d'urgence "trains rentrés" [Study and Characterization of Wear and Heat Phenomena for Aircraft's Structural Materials during Wheels-up Emergency Landings], PhD thesis, École Centrale de Lille, Lille, 2021 [in French].

[6] M. Godet, The third-body approach: A mechanical view of wear, Wear, Vol. 100, No. 1-3, 1984, pp. 437-452, DOI: 10.1016/0043-1648(84)90025-5

[7] M. Godet, Y. Berthier, J. Lancaster, L. Vincent, Wear modelling: Using fundamental understanding or practical experience?, Wear, Vol. 149, No. 1-2, 1991, pp. 325-340, DOI: 10.1016/0043-1648(91)90383-6

[8] G. Zambelli, L. Vincent, Matériaux et contacts: Une approche tribologique [Materials and Contacts: A Tribological Approach], Presses Polytechniques et Universitaires Romandes, Lausanne, 1998.

[9] Y. Berthier, Maurice Godet's third body, Tribology Series, Vol. 31, 1996, pp. 21-30, DOI: 10.1016/S0167-8922(08)70766-1

[10] A.M. Kirk, P.H. Shipway, W. Sun, C.J. Bennett, Debris development in fretting contacts – Debris particles and debris beds, Tribology International, Vol. 149, 2020, Paper 105592, DOI: 10.1016/j.triboint.2019.01.051

[11] K. Kato, K. Adachi, Wear mechanisms, in B. Bhushan (Ed.), Modern Tribology Handbook, CRC Press, Boca Raton, 2000, pp. 273-300.

[12] P.J. Blau, A model for run-in and other transitions in sliding friction, Journal of Tribology, Vol. 109, No. 3, 1987, pp. 537-543, DOI: 10.1115/1.3261499

[13] P.J. Blau, Elevated-temperature tribology of metallic materials, Tribology International, Vol. 43, No. 7, 2010, pp. 1203-1208, DOI: 10.1016/j.triboint.2010.01.003

[14] ASTM G115-10, Standard Guide for Measuring and Reporting Friction Coefficients, 2010.

[15] V. Saikko, Wear and friction properties of prosthetic joint materials evaluated on a reciprocating pin-on-flat apparatus, Wear, Vol. 166, No. 2, 1993, pp. 169-178, DOI: 10.1016/0043-1648(93)90259-O

[16] W. Yuan, G. Dong, Q. Guo, W. Sui, L. Zhang, W. Yuan, Tribological performance of differential gear end-face sliding on washer with a radial groove, Engineering Failure Analysis, Vol. 85, 2018, pp. 126-136, DOI: 10.1016/j.engfailanal.2017.11.015

[17] E. Bergseth, M. Henriksson, S. Dizdar, U. Sellgren, Effects of thrust washer bearing surface characteristics on planetary gear train wear, Wear, Vol. 432-433, 2019, Paper 202933, DOI: 10.1016/j.wear.2019.202933

[18] M. Tikanmäki, P. Sainio, Experiments on friction of dry and wet ice, Cold Regions Science and Technology, Vol. 172, 2020, Paper 102990, DOI: 10.1016/j.coldregions.2020.102990

[19] P. Lepesant, C. Boher, Y. Berthier, F. Rézai-Aria, A phenomenological model of the third body particles circulation in a high temperature

contact, Wear, Vol. 298-299, 2013, pp. 66-79, DOI: 10.1016/j.wear.2012.08.019

[20] N.A.M. Tahir, M.F.B. Abdollah, R. Hasan, H. Amiruddin, The effect of sliding distance at different temperatures on the tribological properties of a palm kernel activated carbon-epoxy composite, Tribology International, Vol. 94, 2016, pp. 352-359, DOI: 10.1016/j.triboint.2015.10.001

[21] U. Olofsson, M. Tu, O. Nosko, Y. Lyu, S. Dizdar, A pin-on-disc study of airborne wear particle emissions from studded tyre on concrete road contacts, Wear, Vol. 410-411, 2018, pp. 165-172, DOI: 10.1016/j.wear.2018.06.012

[22] K.P. Lijesh, M.M. Khonsari, S.V. Kailas, On the integrated degradation coefficient for adhesive wear: A thermodynamic approach, Wear, Vol. 408-409, 2018, pp. 138-150, DOI: 10.1016/j.wear.2018.05.004

[23] Y. Lyu, E. Bergseth, J. Wahlström, U. Olofsson, A pin-on-disc study on the tribology of cast iron, sinter and composite railway brake blocks at low temperatures, Wear, Vol. 424-425, 2019, pp. 48-52, DOI: 10.1016/j.wear.2019.01.110

[24] P. Jayashree, S. Turani, G. Straffelini, Effect of temperature and sliding speed on the dry sliding behavior of a SiC-graphite composite against martensitic steel, Wear, Vol. 450-451, 2020, Paper 203242, DOI: 10.1016/j.wear.2020.203242

[25] M. Leonardi, M. Alemani, G. Straffelini, S. Gialanella, A pin-on-disc study on the dry sliding behavior of a Cu-free friction material containing different types of natural graphite, Wear, Vol. 442-443, 2020, Paper 203157, DOI: 10.1016/j.wear.2019.203157

[26] P. Zhang, L. Zhang, D. Wei, P. Wu, J. Cao, C. Shijia, X. Qu, Substance evolution and wear mechanism on friction contact area of brake disc for high-speed railway trains at high temperature, Engineering Failure Analysis, Vol. 111, 2020, Paper 104472, DOI: 10.1016/j.engfailanal.2020.104472

[27] Y. Desplanques, O. Roussette, G. Degallaix, R. Copin, Y. Berthier, Analysis of tribological behaviour of pad-disc contact in railway braking: Part 1. Laboratory test development, compromises between actual and simulated tribological triplets, Wear, Vol. 262, No. 5-6, 2007, pp. 582-591, DOI: 10.1016/j.wear.2006.07.004

[28] P.J. Blau, Interpretations of the friction and wear break-in behavior of metals in sliding contact, Wear, Vol. 71, No. 1, 1981, pp. 29-43, DOI: 10.1016/0043-1648(81)90137-X

[29] E.A.T. Davin, A.-L. Cristol, A. Beaurain, P. Dufrénoy, N. Zaquen, Differences in wear and material integrity of NAO and low-steel brake pads under severe conditions, Materials, Vol. 14, No. 19, 2021, Paper 5531, DOI: 10.3390/ma14195531

[30] I. Hager, Behaviour of cement concrete at high temperature, Bulletin of the Polish Academy of Sciences: Technical Sciences, Vol. 61, No. 1, 2013, pp. 145-154, DOI: 10.2478/bpasts-2013-0013

[31] A.B. Woodland, A.V. Girnis, V.K. Bulatov, G.P. Brey, H.E. Höfer, Breyite inclusions in diamond: Experimental evidence for possible dual origin, European Journal of Mineralogy, Vol. 32, No. 1, 2020, pp, 171-185, DOI: 10.5194/ejm-32-171-2020